Polymer Testing 128 (2023) 108207

Contents lists available at ScienceDirect

Polymer Testing

journal homepage: www.elsevier.com/locate/polytest

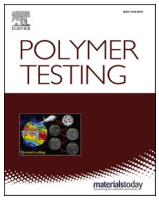

Statistical-based optimization of fused filament fabrication parameters for short-carbon-fiber-reinforced poly-ether-ether-ketone considering multiple loading conditions

Willian S. de Carvalho [a,*], Francesco Marzemin [a], Carlos Belei [a], Sandra Petersmann [b,1], Florian Arbeiter [b], Sergio T. Amancio-Filho [a,**]

[a] Graz University of Technology – TU Graz, Institute of Materials Science, Joining and Forming, BMK Endowed Professorship for Aviation, Kopernikusgasse 24/1, 8010, Graz, Austria

[b] Montanuniversitaet Leoben – MUL, Institute of Materials Science and Testing of Polymers, Otto Glöckel-Straße 2/II, 8700, Leoben, Austria

ARTICLE INFO

Keywords:
Fused filament fabrication
Experimental design
Parameter optimization
Central composite design
Mechanical properties
Polymer characterization

ABSTRACT

Fused filament fabrication (FFF) is one of the most widely used additive manufacturing processes and allows the production of complex parts. FFF can manufacture lightweight and strong structural components when processing high-performance carbon-fiber-reinforced thermoplastics. Although the process feasibility for printing 20% short-carbon-fiber reinforced PEEK was already demonstrated in the literature, a systematic study addressing the influence of printing parameters on different loading conditions is still lacking. Therefore, the present study investigates the influence of selected FFF parameters – i.e., layer height (LH), printing temperature (PT) and printing speed (PS) – on three mechanical properties: tensile (UTS), bending (UBS), and impact (UIS) ultimate strengths. The analyzed samples were printed and tested according to a central composite design of experiments, and each parameter's individual and combined effects were assessed by analysis of variance (ANOVA). Different regression models were obtained for each test, allowing the optimization of the parameters for each condition and resulting in three distinct optimized parameter sets. The relationship between parameters and microstructure was also assessed via fractography analyses, showing that lower LH and PS reduce the number and size of volumetric defects observed within the printed parts, as lower values improve interlayer cohesion. Contrarily, PT showed that average values (around 385 °C) benefit the microstructure the most, as higher temperatures result in larger defects and low temperatures reduce interlayer cohesion. Finally, the contour plots of the three produced models were overlaid to identify a universal parameter set capable of simultaneously correlating and maximizing all three performances. This procedure allowed the identification of the following optimized values: LH of 0.1 mm, PT of 385 °C and PS of 17.5 mm/s, resulting in the experimental UTS, UBS and UIS values of 116.7 ± 5 MPa, 167.2 ± 11 MPa and 28.2 ± 3 kJ/m^2.

1. Introduction

Additive manufacturing (AM) processes have been developed rapidly in diverse application fields due to their layer-by-layer building principle, which allows for significantly reduced costs by decreasing material waste and energy consumption [1,2]. AM processes can be employed for manufacturing complex lightweight parts with optimized topology and without molds, which are required in many polymer processing techniques [3]. Due to their capability to manufacture parts in a single step, production cycles are considerably shortened, improving supply chain efficiency [4]. The attributes mentioned above make AM techniques highly valued, finding applications in aerospace, automobile, engineering, medical, and other related industries [1,3,5–10]. However, it is important to highlight that the properties of additively manufactured parts depend highly on the printing parameters used and that a proper selection of these parameters is an important step in their application [11,12].

AM of lightweight metallic alloys currently has the highest share of

* Corresponding author.
** Corresponding author.
E-mail addresses: willian.salesdecarvalho@student.tugraz.at (W.S. de Carvalho), sergio.amancio@tugraz.at (S.T. Amancio-Filho).
[1] Present address: Carinthia University of Applied Sciences – CUAS, ADMiRE Research Center, Europastrasse 4, 9524 Villach – Austria.

https://doi.org/10.1016/j.polymertesting.2023.108207
Received 15 June 2023; Received in revised form 9 September 2023; Accepted 13 September 2023
Available online 15 September 2023

aviation-related applications, as the produced parts present high strength-to-weight and reduced buy-to-fly ratios [13]. However, whether processed by AM or not, the use of engineering polymers has also gained momentum in recent decades, since their processing is generally far easier due to the lower energy consumption, low reactivity of the feedstock to the surrounding environment and even potentially superior mechanical properties (especially when reinforced) [14–19]. While thermoset-based composites continue to dominate the market, there is a growing trend towards using thermoplastics, which present advantages such as no need for curing stages, increased impact toughness, and recyclability [20,21].

Among several different polymer AM techniques developed over the years, fused filament fabrication (FFF) is one of the most popular for thermoplastics due to its simplicity, versatility, affordability and commercial availability [22]. These advantages recently turned FFF technology into an attractive industrial process, which has proved itself as a batch production solution, extending beyond merely exclusive use for prototyping [23,24].

The FFF process uses a filament that is fed into a heated nozzle as a feedstock, where the material reaches a semi-solid viscous state. Then, a well-defined material quantity is extruded through the nozzle and deposited onto the building plate. The relative movement of the nozzle with respect to the building plate is controlled by a sequential programming code, which defines the shape of the deposited layer. The layer deposition is repeated several times, one on top of another, enabling the production of complex geometries with high accuracy [5,23,25,26]. Fig. 1 depicts an overview of the FFF process.

The versatility of this process is demonstrated in its capability to print under multiple conditions — including zero-gravity environments [27] — and the broad selection of available materials. These materials range from general use (e.g. PLA, TPU, PVA and PET) to engineering (e.g. PA, ABS, TPU, PET and POM) thermoplastics [25,28–31]. Additionally, the FFF processability of short [7] and continuous [32] carbon fiber-reinforced polymers was already demonstrated. However, despite the vast number of materials available, most present limited chemical resistance, durability and mechanical properties. Nevertheless, the recent development of new high-temperature printers enabled the FFF process of high-performance thermoplastics, such as PEEK, PVDF, PEKK, PEI, and PPS [28,33], which are less susceptible to the drawbacks mentioned above.

Among the available high-performance thermoplastic filaments for FFF, poly-ether-ether-ketone (PEEK) draws particular interest, since it presents many remarkable properties [23]. Thanks to its structure, this semi-crystalline high-performance thermoplastic from the poly (aryletherketone) (PAEK) family exhibits superior thermal resistance and mechanical performance, plus a low linear expansion coefficient and chemical stability [34]. Due to its high Young's modulus, tensile strength, and low specific density, PEEK is considered a suitable candidate to replace aluminum and steel alloys in a wide range of applications, especially in the aerospace and automotive sectors [6,17,18,35]. Furthermore, since PEEK shows biocompatibility and radio-transparency, it is a promising material to replace metals in biomedical applications, such as implants [36,37], surgical instruments and dental devices [38].

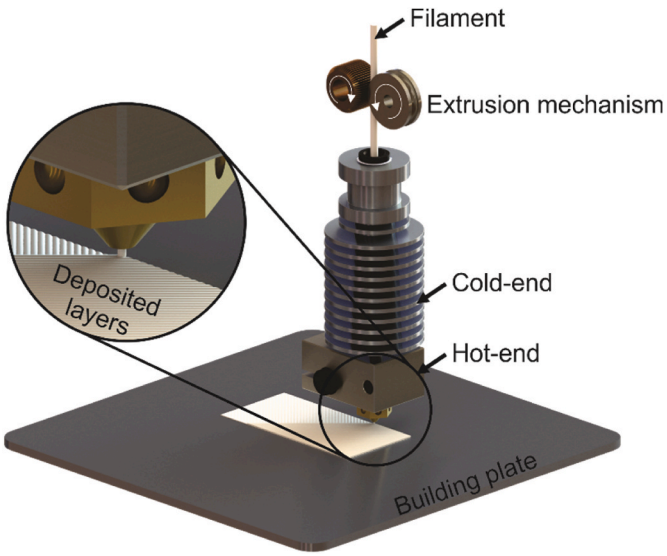

Fig. 1. A schematic representation of the FFF process.

As Wang et al. [4] reported, incorporating reinforcements in PEEK filaments is an additional strategy to enhance the mechanical performance of the 3D-printed parts. The combination of PEEK and reinforcement aims to exploit the synergistic effects of both constituents, by creating a material with superior and tailored properties. In this scenario, short carbon fibers (CF) are arguably the most used and studied reinforcement for high-performance FFF-printed components, since they can improve the overall mechanical performance of a printed part, including tensile, bending and impact strengths [4,39]. Additionally, at the same wt.%, short-carbon-fiber reinforced PEEK (PEEK-CF), achieves higher tensile strength than short-glass-fiber reinforced PEEK (PEEK-GF) [4]. Finally, using short-carbon fibers is an affordable way to enhance the performance of PEEK and other thermoplastics. It is a more cost-effective alternative to using long or continuous fibers, which require complex and expensive printing systems [7].

Although promising, the FFF processing of PEEK-CF parts remains a complex task, since the process parameters strongly affect features such as printing quality, mechanical properties, building time and the final costs of an FFF-produced component [4]. Other relevant factors in the process include filament quality, fiber orientation, printing devices, environmental conditions (temperature, humidity) and others [3]. Therefore, selecting an optimized combination of parameters is vital when processing PEEK-CF via AM. As such, a few authors devoted their efforts to studying PEEK-CF processed by FFF [4,40]. Despite the extensive coverage provided by these studies, there is still a need for a comprehensive analysis of the intricate interactions between printing parameters, microstructure and the mechanical properties of FFF PEEK-CF, especially when considering multiple loading conditions. Moreover, the influence of carbon fibers on the material processability is still unclear.

In the context of these gaps to be filled, the present study proposes optimizing the FFF parameters for 20%-short-carbon-fiber reinforced PEEK (PEEK-20CF) to concomitantly improve three different and individual mechanical responses: the ultimate tensile, the bending and the impact strengths. The analyzed samples were printed and tested according to a central composite design of experiments (DoE), and each parameter's individual and combined effects were assessed by analysis of variance (ANOVA). Reliable regression models were obtained for each test, allowing the optimization of the parameters for each condition and resulting in three different optimal parameter sets. The obtained models were used to produce contour plots for the individual responses, which were later overlaid to identify a range of parameters set capable of simultaneously correlating and maximizing all three performances. Finally, the relationship between parameters and microstructure was also evaluated via fractography analyses, showing that a proper selection of 3D-printing parameters can drastically reduce the amount and size of defects in the printed part.

2. Experimental procedure

2.1. Base materials and FFF process setup

The testing specimens used in this study were produced via FFF using a 1.75-mm-diameter PEEK-20CF filament supplied by 3DXTech (Grand Rapids, MI, USA). As recommended by the manufacturer, the filament

was dried at 120 °C for 4 h before printing to eliminate the absorbed moisture [41]. Table 1 presents different physical and mechanical properties expected for the material according to the manufacturer.

A Funmat HT Enhanced printer (Intamsys, Shanghai, China) for high-temperature polymers was used to manufacture the specimens. This printing system has a maximum nozzle temperature of 450 °C and is equipped with a heated building plate and chamber capable of reaching temperatures up to 160 °C and 90 °C, respectively. In the present study, the building plate and chamber temperatures were fixed at 160 °C and 90 °C, respectively, as Qu et al. [42] demonstrated that both maximum temperatures improved the interlayer bonding force and mechanical performance of PEEK material produced using the same printer. Additionally, a V6 hardened steel nozzle produced by E3D (Oxford, UK) was used to improve the nozzle lifespan, as the abrasive behavior of reinforcing fibers leads to internal nozzle wear during the FFF process, which can result in process instability [43].

FFF equipment allows the user to control dozens of parameters; however, optimizing all the available parameters simultaneously would be challenging, given the extensive number of tests necessary. Therefore, this study adopted constant pre-set values for different FFF parameters, as listed in Table 2. The main variable parameters used in the optimization step will be presented and discussed in the following section.

Prior to the printing process of the specimens, a thin layer of polyvinyl-pyrrolidone (PVP) glue supplied by deli (Ningbo, China) was spread over the glass platform to improve the adhesion of the first printed layers to the platform. After that, the composite parts were printed with a brim to improve the adhesion further and ensure a continuous and stable material flow at the beginning of each printing part.

2.2. FFF parameters optimization and mechanical testing

The mechanical properties of printed parts depend highly on their achieved microstructure and, consequently, the printing parameters used. Therefore, identifying a set of optimized parameters is essential to produce strong FFF components. This study optimized three main FFF parameters via design of experiments (DoE) to maximize their quasi-static mechanical performance. DoE represents an effective method to yield process parameters optimization by evaluating process variables' effects on desired responses [44,45], and its efficiency in optimizing FFF parameters has been proven in several publications [7,46,47]. A central composite design (CCD) model with three factors, i.e. three process parameters – layer height (LH), printing temperature (PT), and printing speed (PS) – was followed to analyze their influence on three responses from different testing conditions: ultimate tensile strength (UTS), ultimate bending strength (UBS) and unnotched impact strength (UIS). CCD is among the most popular classes of DoEs due to its efficiency and good fitting capability with second-order models. These advantages are achieved by exploring the combination of the cube and axial points around the generated optimization matrix, allowing the user to test not only moderate parameters, but also the combination of extreme values near the limits of the applied equipment. Consequently, the CCD model is considered more robust than other methods, such as the Box-Behnken design [44].

The range values used for LH, PT and PS in the optimization process were based on preliminary screening investigations and the published literature [8], and are presented in Table 3. As it will be later described, PT was determined based on the thermal behavior of the material.

The levels of the used model were defined with the extreme values representing axial points to explore values at the printer's limits. As three process parameters are used, the CCD model recommended 15 combinations. A graphical illustration of the generated cube with the proposed combinations and ranges is presented in Fig. 2. Four additional center point replicas and five validation points were printed and tested for all the conditions to increase the model's reliability and accuracy to predict the performance of different points within the analyzed parameters range [48,49]. The exactly values for those points will be later presented in the text. Therefore, 24 samples were produced for each mechanical test, and the specific values and results achieved will be presented later.

Fig. 3-(a) presents the dimensions of the tensile samples used in this study, which were in accordance with the Type 1BA of the ISO 527 standard [50]. Bending samples were produced according to ISO 178 [51], while unnotched impact specimens followed ISO 179 [52]. ISO 178 and 179 share the same dimensions and are presented in Fig. 3-(b). Slicing was carried out using the UltiMaker Cura software (Utrecht, The Netherlands), where each specimen's process parameters were defined.

All the samples were printed in random order and cooled to room temperature inside the printer. Tensile specimens were tested at a constant speed of 1 mm/min in a Zwick Z100 universal testing machine

Table 2
Selected FFF parameters applied for PEEK-20CF.

Printing parameters	Values
Nozzle diameter [mm]	0.4
Infill density [%]	100
Wall thickness [mm]	0.8
Infill pattern	Lines
Road angle [°]	−45/+45
Overlap interval [mm]	0

Table 3
FFF parameters analyzed and their selected levels.

Parameter	Abbreviation	Minimum	Maximum
Layer height [mm]	LH	0.1	0.3
Printing temperature [°C]	PT	360	420
Printing speed [mm/s]	PS	5	30

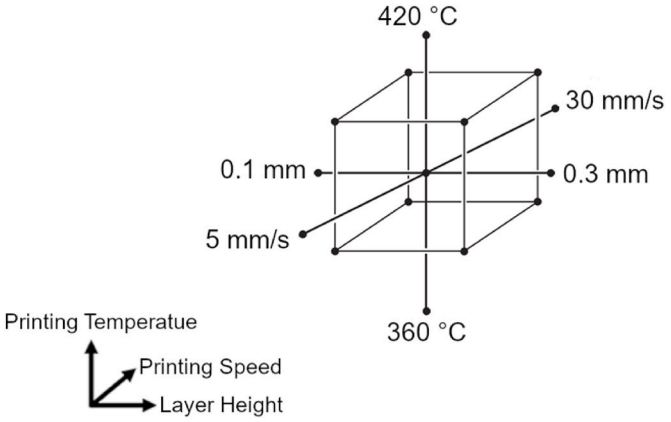

Fig. 2. Visual representation of the proposed CCD, consisting of eight cubic points, six axial points, and one center point. Each coordinate represents a combination of parameters.

Table 1
Selected physical and mechanical properties of FFF PEEK-20CF [41].

Material	Density [g/cm^3]	Tensile strength [MPa]	Tensile modulus [MPa]	Elongation at break [%]	Flexural strength [MPa]	Flexural modulus [MPa]
PEEK-20CF	1.39	126	10100	1.9	145	11200

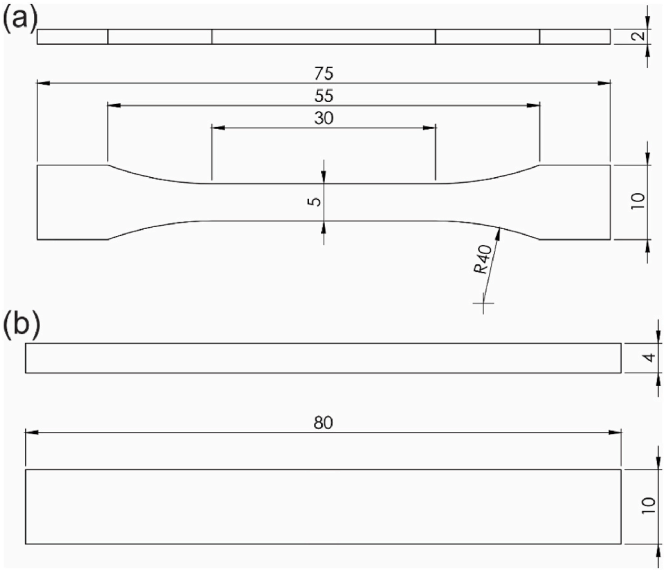

Fig. 3. Dimensions (in mm) of the used specimens for (a) ISO 527 tensile and (b) ISO 178 bending and ISO 179 unnotched impact testing.

(Zwick/Roell Group, Ulm, Germany) with a 100 kN load cell. Bending samples were also tested with a constant speed of 1 mm/min in an AGS-X universal bench test machine with a 5 kN load cell manufactured by Shimadzu (Kyoto, Japan). Finally, Charpy impact tests were carried out on unnotched specimens at 23 °C using a HIT25/50P pendulum impact tester manufactured by Zwick/Roell Group (Ulm, Germany) and equipped with a 7.5 J pendulum. All the samples were tested in their as-built condition to maximize their mechanical performance and avoid additional post-treatment steps, such as annealing of the parts. Therefore, a deep analysis of the influence of post-treatment processes on the microstructure, crystallinity degree and mechanical properties of the parts is out of the scope of this study and will be published in a separate manuscript.

The obtained results were used to generate different models to predict UTS, UBS and UIS within the analyzed ranges, and analysis of variance (ANOVA) was applied to them using a confidence level of 95% (i.e., $\alpha = 0.05$), to evaluate their capabilities for determining the statistically significant factors (main and interactions). The models were also applied to create contour plots which supported the identification of optimized parameters considering the individual mechanical responses. Finally, the contour plots were superimposed, creating an overlaid contour plot capable of identifying a range of optimized parameter combinations. The efficacy of overlaid contour plots in such complex optimizations was successfully reported in the literature for other materials and manufacturing processes [53–55].

2.3. Microscopical, thermal and fractography analyses

Before the optimization process, the PEEK-20CF filament was characterized to assess its quality, fiber-matrix adhesion and fiber length distribution. Random as-received filament segments were cut, embedded in Epofix resin (Struers, Ballerup, Denmark), polished following standard materialography steps and analyzed transversally and longitudinally via light optical microscopy (LOM) using an Axio Observer light optical microscope (ZEISS, Oberkochen, Germany). Selected printed and polished samples were also analyzed using the same equipment to evaluate the influence of the printing parameters on the material microstructure.

The thermal decomposition behavior of the filament was also investigated via thermogravimetric analyses (TGA) using a TGA/DSC 1 equipment produced by Mettler Toledo (Columbus, USA). The examinations were performed on 9.5 mg (±0.5 mg) of PEEK-20CF specimens in an inert nitrogen atmosphere. The samples were heated from room temperature up to 1000 °C using a heating rate of 10 °C/min and a flow rate of 35 ml/min. The results support the definition of the PT range used in the optimization step.

Finally, selected samples were analyzed via scanning electron microscopy (SEM) using a TESCAN Mira 3 microscope (Brno, Czech Republic) to investigate and understand the influence of the analyzed FFF printing parameters on the microstructure and, consequentially, the mechanical behavior of the printed samples. Tested tensile specimens were used for this purpose, where the fractured surface was analyzed. Prior to the analyses, the exposed surfaces were carbon sputtered and the sputtered surfaces were observed using the secondary electron detector with an acceleration voltage of 5 kV, at a working distance of 50 mm and a chamber pressure of 10^{-1} Pa.

3. Results and discussion

3.1. General aspects of PEEK-20CF filament

Initially, general aspects of the filament used in the present study are addressed. As Gao et al. [56] presented, the filament quality (i.e. residual porosity, fiber length distribution, etc.) used in the FFF process directly impacts the achieved properties of the printed parts. Fig. 4 shows the microscopic analyses of the as-received PEEK-20CF filament perpendicularly and along the extrusion direction.

Fig. 4-(a) shows that the used filament presents a high availablitiy level of residual porosity. A close-up is presented in Fig. 4-(b), where one can observe that the apparent porosities are much bigger than the CF. The analysis of the filament along its main axis is presented in Fig. 4-(c), showing that the porositis are elongated in this direction. This porosity orientation indicates that these volumetric defects were introduced during filament production. Additionally, it is possible to observe that the size of the pores varies significantly, reaching values close to 100 μm. As reported in the literature, the presence of this kind of defect in CF-reinforced polymers, such as PEEK [57], ABS [58,59] and PLA [60], results from issues during the filament production. A few reasons are residual moisture in the fibers, problems related to the extrusion parameters or poor adhesion between the thermoplastic matrix and the CF surface during the filament fabrication [60]. The presence of such

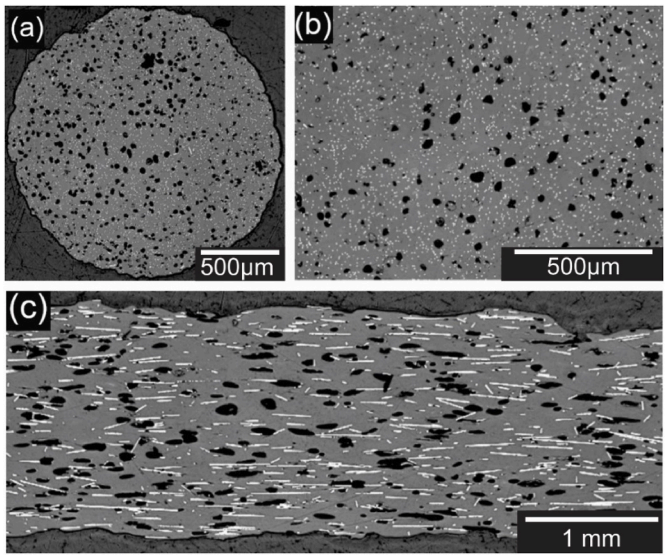

Fig. 4. Microscopic analysis of the as-received filament: (a) shows a full section of the filament observed perpendicular to the extrusion direction, (b) a close-up of the filament observed perpendicular to the extrusion direction and (c) shows a view of the filament along the printing direction.

volumetric defects has a major influence on the failure mechanisms of FFF parts and, consequently, on its mechanical performance. Furthermore, high porosity may reduce the amount of extruded material, as FFF printers do not account for their presence, affecting the geometry and density of the printed components.

In addition to defects, the characteristics of the CFs also strongly influence the mechanical properties achieved by the printed parts, such as their orientation and aspect ratio. Fig. 4 shows that the fibers have an average diameter of 7 ± 0.5 μm and are aligned parallel to the filament's central axis, enhancing their load strength in this direction. Distribution in the fiber length can also be observed, and it was quantified via image analysis. The obtained histogram is illustrated in Fig. 5, where more than 1300 fibers were measured automatically.

Fig. 5 shows that the average fiber length in the used filament is 59.7 μm, where 90% of the fibers are shorter than 100 μm. Since the mechanical properties of CFRPs mainly depend on the fiber length, it is possible to highlight that using such short fibers hinders the full potential of FFF PEEK-20CF. As Ning et al. [59] observed, using longer fibers improves the mechanical performance of printed parts, but one may consider that longer fibers might be difficult to extrude using standard nozzles due to their small diameter. A further increment in the fiber content would have a similar effect; however, more than 20% of CFs in the PEEK matrix is unsuitable for FFF process, as the melt viscosity reached would be too high to be extruded using the commercial printers available [40].

Finally, the PEEK-20CF filament was also thermally characterized via TGA to support selecting the PT range used in the optimization phase, ensuring that the selected temperatures will not decompose the PEEK matrix, diminishing the composite properties. The obtained curve is presented in Fig. 6.

According to Fig. 6, the polymer undergoes thermal decomposition in two stages, with the onset at around 550 °C. The initial stage is characterized by a rapid and significant mass loss, resulting in the volatilization of around 35% of the polymer mass. This phase occurs up to approximately 600 °C and is caused by the random chain scission of the ether and ketone bonds [61]. The second stage follows above 600 °C and continues up to about 800 °C. This decomposition phase is due to the cracking and dehydrogenation of the crosslinked residue formed during the first phase, resulting in a thermally stable carbonaceous char [62]. During this phase, mass loss is linked to the loss of phenol groups [63], as well as the production of carbon monoxide (CO) and carbon dioxide (CO_2) [64]. There is minimal further mass loss observed between 800 °C and 900 °C, demonstrating the material's high thermal stability. Therefore, based on the filament manufacturer's

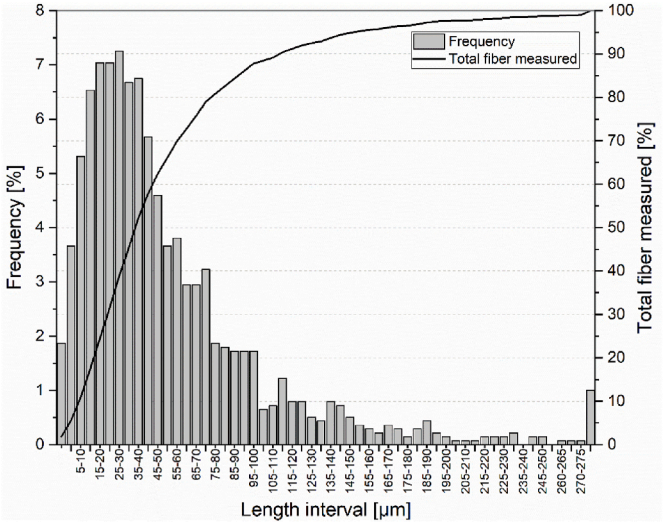

Fig. 5. Fiber length distribution of the as-received PEEK-20CF filament.

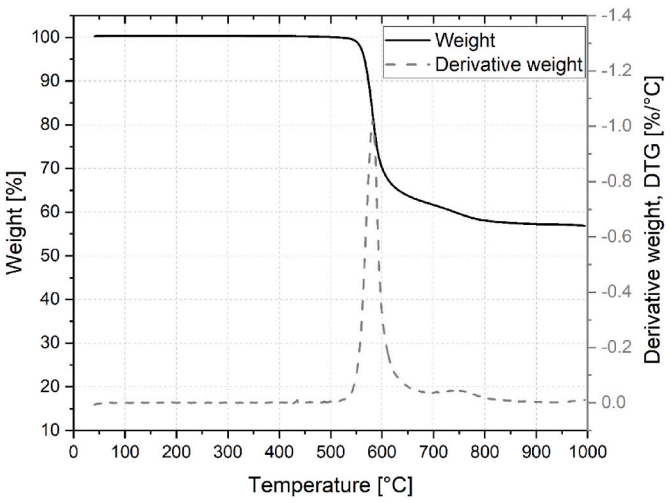

Fig. 6. Representative TGA curve obtained for the PEEK-20CF filament.

recommendations [41] and the presented temperatures, the PT range was defined from 360 to 420 °C to avoid any sign of polymer decomposition and extreme temperatures inside the printer.

3.2. Process parameters optimization

24 samples were printed and tested under three different loading conditions (tensile, bending and impact). From each test, the failure strength was used as the analyzed response. The obtained results are presented in Table 4, where the first 19 samples represent the CCD parameters combination matrix (MP) with the five central points (CP), and the last five are the validation points (VP) in which different combinations of parameters were used to test the capability of the produced prediction model.

The results presented in Table 4 indicate that despite the parameter values used in this study being within the ranges recommended by the filament supplier, the UTS, UBS and UIS values varied considerably from one condition to another, demonstrating the importance of parameter optimization. The regression analysis of each response resulted in

Table 4
CCD parameter matrix and UTS, UBS and UIS experimental results.

Points	LH [mm]	PT [°C]	PS [mm/s]	**UTS [MPa]**	**UBS [MPa]**	**UIS [kJ/m²]**
MP	0.25	408	10	83.7	156.5	25.1
MP	0.2	390	30	89.1	141.9	30.5
MP	0.2	420	17.5	83.5	155.1	26.7
MP	0.2	360	17.5	92.8	127.7	28.4
MP	0.2	390	5	102.4	160.5	28.2
CP	0.2	390	17.5	98.5	150.2	30.5
CP	0.2	390	17.5	93.6	154.1	30.9
MP	0.15	375	10	107.6	146.9	25.1
CP	0.2	390	17.5	95.5	153.4	31.6
MP	0.1	390	17.5	117.3	132.7	26.6
CP	0.2	390	17.5	96.5	152.2	30.5
MP	0.15	375	25	105.0	129.7	34.7
MP	0.15	408	25	105.3	158.3	21.2
CP	0.2	390	17.5	97.0	152.2	25.8
MP	0.25	408	25	87.3	140.3	20.0
MP	0.3	390	17.5	84.8	146.5	25.4
MP	0.25	375	25	84.6	136.9	33.0
MP	0.15	408	10	110.3	181.5	27.4
MP	0.25	375	10	96.4	146.2	21.8
VP	0.1	400	20	111.3	154.6	26.1
VP	0.25	395	15	94.7	146.8	25.1
VP	0.3	415	10	104.8	162.6	20.1
VP	0.2	380	25	110.3	128.8	36.5
VP	0.15	385	5	107.7	158.3	23.1

different quadratic models capable of predicting the individual mechanical behaviors of the printed specimens. Depending on the dataset obtained, full models can be obtained and used; however, as described by Myers et al. [44], one can apply reduced models for certain studies as a tentative to simplify the equations and highlight their influences. Therefore, this study used reduced models obtained via backward elimination with an $\alpha = 0.05$. The obtained reduced models for UTS, UBS and UIS are represented by Equations (1)–(3), where the responses are a function of the statistical printing parameters. In addition, the ANOVA also provides relevant information by assessing the contribution percentage of each parameter effect via weighted p-values. Therefore, terms with a p-value lower than 0.05 were considered statistically significant for the present study. The obtained p-values are presented in Table 5, where the values for the relevant interactions and all main effects (LH, PT and PS) were included. The missing values were for interactions considered not relevant to the analyzed responses.

$$UTS = -938 - 414*LH + 5.72*PT - 0.384*PS + 630*LH^2 - 0.00745*PT^2 \quad (1)$$

$$UBS = -490 + 2297*LH + 1.687*PT - 0.949*PS - 5.93*LH*PT \quad (2)$$

$$UIS = -152.7 + 153*LH + 11.7*PS + 0.423*PT - 417*LH^2 - 0.02966*PS*PT \quad (3)$$

The p-value analyses show that different printing parameters are relevant for each analyzed response: LH and PS main, and LH^2 and PT^2 second-order interaction effects were relevant for UTS; PT and PS main, and LH*PT two-way interaction effects were relevant for UBS; PT main and PT*PS two-way interaction effects were relevant for UIS. The relative magnitude and the contribution to the analyzed responses of each effect can be translated and plotted into Pareto charts to simplify understanding of them. Fig. 7 presents these charts.

The Pareto charts show bars the lengths of which are directly proportional to the standardized effect of each parameter or interaction, meaning that the effects of the analyzed parameters and interactions are divided by their standard error, and then presented in descending order of significance. A vertical dashed line is included in the chart to indicate the relevance threshold, which separates the statistically significant parameters at a 95% confidence level. Therefore, any bar intersecting this line corresponds to a statistically significant effect for the considered responses.

Fig. 7-(a) highlights that PT is the only linear parameter with no statistical relevance to UTS, while LH^2 and PT^2 are the relevant second-order interaction effects. Here no two-way interaction effect was found to be significant. LH presented an extreme magnitude, meaning that it is the most relevant factor and small changes in its value can strongly influence UTS. Similar effects were identified in the literature [4]. On the other hand, Fig. 7-(b) shows that PT and PS are significant to UBS, contrarily to LH and the behavior observed for UTS. As Wang et al. [4] observed, the PT and PS effects counteract the statistical impact of LH for UBS compared to UTS, which explains the reduction in LH's relevance. Similarly to UBS, Fig. 7-(c) shows that UIS depends to a major extent on PT, but PS does not reach the relevance threshold. Additionally, the magnitude presented by the bars in Fig. 7-(b) and -(c) indicate a lower relevance of the analyzed parameters on UBS and UIS, respectively, than on UTS. A detailed discussion of these effects, together with their respective synergic (positive) or non-synergic (negative) behavior, is presented in the following sections.

Table 5
Obtained p-values for the effects of the relevant parameters and their interactions considering UTS, UBS and UIS.

	UTS	UBS	UIS
LH	<0.001	0.648	0.208
PT	0.104	<0.001	0.015
PS	0.008	0.002	0.143
LH^2	0.028	–	0.028
PT^2	0.021	–	–
PS^2	–	–	–
LH*PT	–	0.027	–
LH*PS	–	–	–
PT*PS	–	–	<0.001

The obtained equations (Equation (1) – (3)) also allow a comparison between the predicted values of UTS, UBS and UIS against their respective experimental results. The comparison for all three conditions is presented in Fig. 8, where the additional five randomly produced validation points (presented in Table 4) for each condition are also displayed. Additionally, the obtained standard error (S), R-squared (R-sq), adjusted and predicted R-sq values were included.

By comparing the predicted and the experimental results, one can observe that almost all data points fall within the 95% confidence interval of the model for all the analyzed responses within the analyzed range. An exception was identified for a central UTS value (Fig. 8-(a)); however, this point is located at the mid-range of the spectrum, close to multiple DoE points within the limits. This information, combined with the high adjusted and predicted R-sq values (88.13 and 79.05%, respectively) obtained for the model, indicates that this point might be an outlier to the general specimen's behavior. On the other hand, UBS (Fig. 8-(b)) and UIS (Fig. 8-(c)) exhibit metrics much lower than UTS, with UBS presenting 68.22 and 50.77% and UIS 68.46 and 48.49% for adjusted and predicted R-sq values, respectively. According to Myers et al. [44], if the adjusted and predicted R-sq differ by less than 20%, this suggests that the model effectively fits the data and can be applied to predict values for other combinations of parameters. However, these values are not in the highest range of accuracy, meaning that the application of the created model must be carefully analyzed and the recommended combinations must be validated by experimental tests.

Despite the shortcomings, the created models had almost all analyzed points within their confidence interval. Therefore, the achieved results can be considered satisfactory, with the models being useful to optimize the parameters, considering the analyzed responses and evaluated parameter ranges. Thus, Equations (1)–(3) were used to create contour plots to illustrate the interaction effects between the parameters, and the obtained graphs are illustrated in Fig. 9. Here two parameters are varied and the third is fixed on the center value.

According to Fig. 9-(a), there is an optimum PT between 380 and 390 °C when considering UTS. It is also clearly presented here that increments in LH and PS reduce the reached UTS values, indicating that the lowest LH and PS values should be used. Fig. 9-(b), on the other hand, indicates that PT values near the explored upper limit (420 °C) result in the highest UBS values. However, low values for LH and PS improved both UBS and UTS. Finally, Fig. 9-(c) shows that UIS behaved completely different from UTS and UBS, being optimized when average LH values (0.15–0.25 mm) were coupled with a high PS. Additionally, opposite behaviors were identified for UIS when comparing LH x PT and PT × PS interactions. When analyzing LH x PT, the contour indicates that a lower PT benefited UIS. However, the PT x PS plot indicates that this statement is applicable only for PS > 15 mm/s, as higher PT is recommended when using PS below this limit.

The results presented in Fig. 9 are partially in accordance with the limited results available in the literature. Wang et al. [4] reported that lower LH always improved UTS, UBS and UIS for PEEK-5CF, but the findings here described show a different behavior for UIS. Additionally, Wang described that a higher PT improved UTS, UBS and UIS values, differing from the behaviors observed for UTS and UIS (when using high PS). A detailed discussion of how these parameters affect the microstructure of the printed parts and consequently, their performance is presented in the following sections.

All the interactions in Fig. 9 exhibit well-defined regions where the responses are maximized. Therefore, by combining these analyses with Equations (1)–(3), different optimized parameter combinations can be identified for each response, where their values are maximized. The optimized values for each condition are summarized in Table 6, together with the predicted and experimental values obtained for each combination.

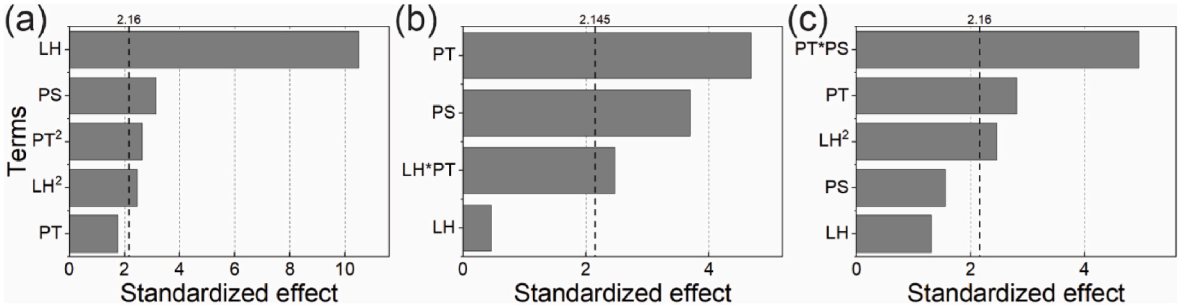

Fig. 7. Pareto chart of the significant factors and interactions effects for (a) UTS, (b) UBS and (c) UIS.

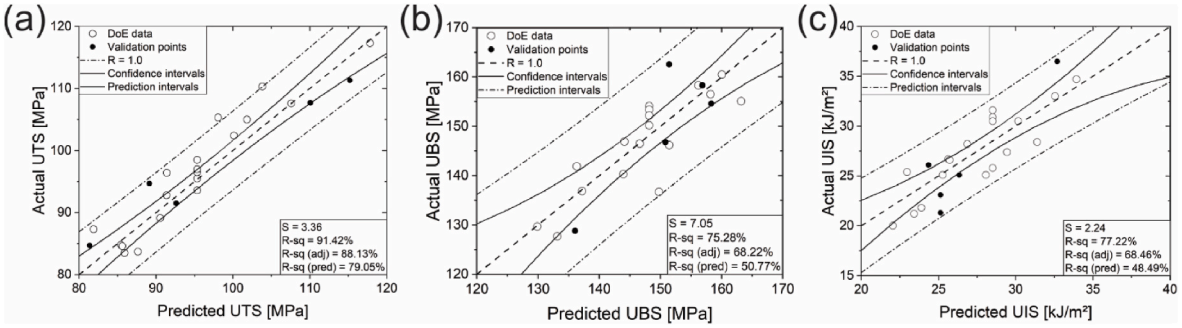

Fig. 8. FFF PEEK-20CF predicted versus actual diagram for (a) UTS, (b) UBS and (c) UIS.

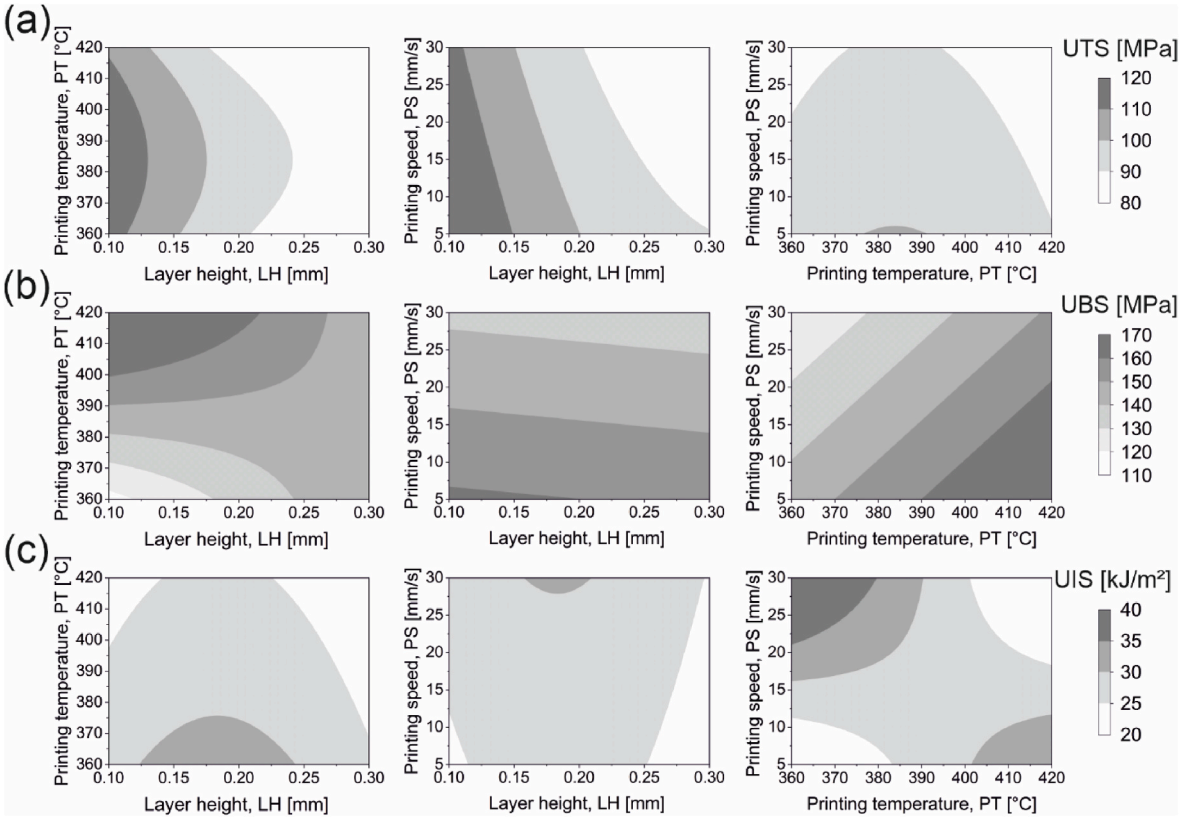

Fig. 9. Contour plots obtained within the optimization process for (a) UTS, (b) UBS and (c) UIS.

The results show that different optimized combinations are obtained for each response analyzed, since it is impossible to maximize two or more responses simultaneously. However, in such multi responses experiments, the contour plots can be superimposed, creating an overlaid graph that can be used to identify a feasible area where the predicted means of all analyzed responses are within an acceptable range [54]. Therefore, an overlaid contour plot was generated, where LH and PT were the independent variables. PS was fixed at the median value of

Table 6
Optimized parameters for each response, including the predicted and the experimental results.

Response	LH [mm]	PT [°C]	PS [mm/s]	Predicted	Experimental
UTS	0.1	385	5	114.4 MPa	120.1 ± 7 MPa
UBS	0.1	420	5	194.8 MPa	179.3 ± 15 MPa
UIS	0.18	360	30	32.4 kJ/m^2	39.2 ± 4 kJ/m^2

17.5 mm/s, as lower values resulted in overlong printing jobs, which would be undesired for industrial applications. Higher PS values were avoided, since these strongly diminish the UTS and UBS values, as described in Fig. 9. The obtained overlaid plot is presented in Fig. 10.

The overlaid plot considered the range between 80% and 100% of the maximum value reported for UTS, UBS and UIS (Table 6). The limits comprehending these ranges result in the optimized white area marked in Fig. 10, where all three responses exceed the 80% mark. Although any set of parameters within this region can be considered optimized, a final combination can be proposed by comparing the optimal process parameter values in Table 6. As previously discussed, optimizing all three responses simultaneously is a complex task, but if two responses are analyzed individually, a set of parameters that keep the third one within the highlighted area can be feasible.

Therefore, since UTS and UBS benefit from lower LH values, the parameter can be kept at its lowest level (0.1 mm) to benefit both responses. Fig. 10 indicates that UIS is optimized with a LH of 0.1 mm and PS of 17.5 mm/s only between a PT of 385 and 400 °C. Since 385 °C also matches the optimized PT value for UTS (Table 6), a PT of 385 °C was selected to benefit UIS and UTS. Therefore, the final set of optimized parameters was defined as a LH of 0.1 mm, PT of 385 °C and PS of 17.5 mm/s, resulting in the experimental UTS, UBS and UIS values of 116.7 ± 5 MPa, 167.2 ± 11 MPa and 28.2 ± 3 kJ/m^2.

In order to investigate in detail the effects of the single parameters on the microstructure of the printed samples, as well as to explain the effects observed along the optimization process, fractography analyses were conducted via SEM. The axial and center points tested under tensile were used for that purpose, as they cover the whole range explored in this study. The obtained results are presented below for each parameter.

3.3. Influence of layer height

Fig. 11 presents the fracture surface of tensile test specimens printed with a PT of 390 °C, PS of 17.5 mm/s and LH of (a) 0.1 mm, (b) 0.2 mm and (c) 0.3 mm. A comparison between the specimens highlights microstructural changes caused by the different LH values. A clear distinction between successive layers can be observed in the lateral

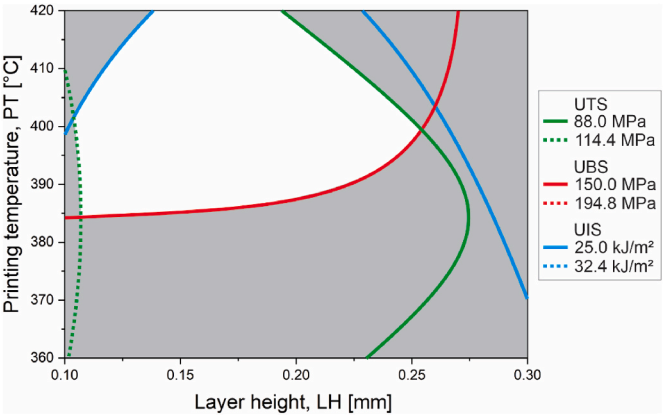

Fig. 10. Overlaid contour plot for UTS, UBS and UIS, considering their maximum predicted value and their 80% as upper and lower limits, respectively.

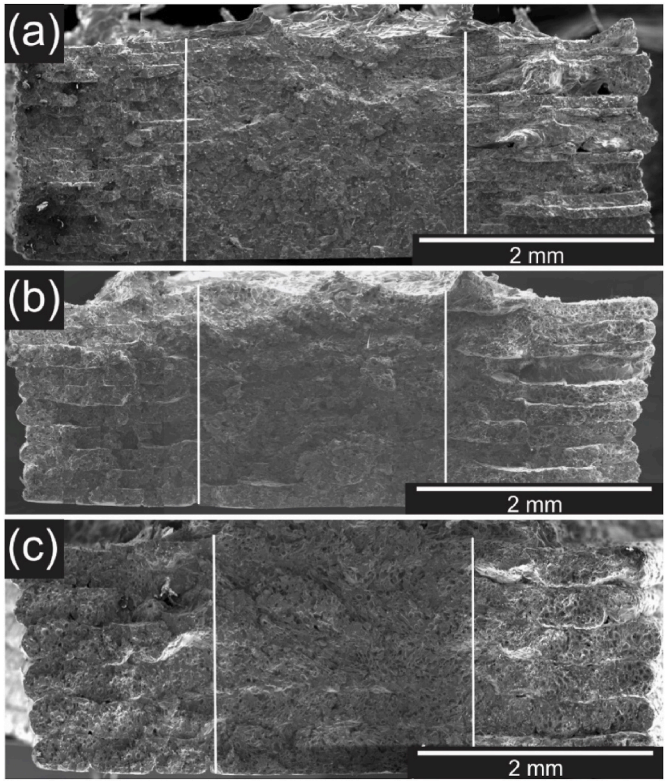

Fig. 11. Fracture surface of tensile tested specimens printed with a PT of 390 °C, PS of 17.5 mm/s and LH of (a) 0.1 mm, (b) 0.2 mm and (c) 0.3 mm.

regions. On the center, however, such a layer-to-layer contrast fades out, with the microstructure being considerably more homogeneous, which is somewhat comparable to a bulk condition.

This effect can be attributed to the different cooling gradients between the sides and the center of the specimen, as the sides isolate the center of the specimen from the relatively colder environment. Therefore, the sides are exposed to a faster cooling rate; if it is too abrupt, the neck growth between adjacent roads will be hindered [65], and the cohesion between the two layers will be suboptimal. It is possible to observe that for more inside regions of the specimens, this does not occur, as the thermal gradient of the central regions is less steep. Consequently, the neck growth is aided, and the layers bond more efficiently [25].

As just described, the microstructural feature could be observed regardless of LH. However, differences across different LH values could also be noticed despite this common aspect. For one, the extension of the bulk region (white lines, Fig. 11) seemed to be slightly larger for LH = 0.1 mm (Fig. 11-(a)) when compared to 0.2 and 0.3 mm (Fig. 11-(b) and Fig. 11-(c), respectively), indicating that low LH appears to improve the interlayer adhesion. This can be explained by the fact that LH is inversely-proportional to the completion time for a given print job, since the printing time for any arbitrary model would increase as the slicing becomes thinner. Consequently, this also implies that the parts remain in the heated chamber and on the heated bed for an inversely proportional period to LH.

Such an increased dwell time during the print job has been shown to enhance interlayer adhesion [4,7,65,66], since the bond formation between two adjacent filaments is a highly temperature-dependent process. Therefore, since low LH specimens required longer printing times, it is reasonable to assume that this fact played a major role in interlayer cohesion. Additionally, it could be argued that with a constant nozzle diameter, a reduction in LH changes the shape of the extrudate from cylindrical to oblong, potentially reducing the voids [67] – that reportedly decrease stiffness and strength – which in turn will increase

the density of the printed components [25].

Finally, the number of pores and defects appeared to be strongly impacted by the LH increment. Sections of untested samples were polished and analyzed under LOM to analyze this behavior and the obtained images are presented in Fig. 12. Here it is possible to observe that samples with higher LH have increased numbers of both defects and pore sizes. These defects (mostly voids) were already observed in the filament in the as-received condition (Fig. 4), since they are a result of poor incorporation of the fibers into the matrix during the filament manufacturing process [58,59,68,69]. Additionally, interlayer voids are also formed between the deposited beads and, despite the pressure incurred by the extrusion through the heated nozzle, they tend to be at least partially retained [4,7]. These voids create stress concentration sites [68] and significantly contribute to the failure of the specimen, as reported elsewhere [39,70]. Furthermore, a loss of directionality in the fibers seems to be caused by the LH increment, although further investigation is needed to assess the extent of this feature in the hereby printed parts, its causes and possible effects.

3.4. Influence of printing temperature

PT is important not only for ensuring the filament's processability but also due to the overall influence on the temperature gradients forming while the part is printed. These gradients impact, among others, cooling rates and therefore features such as interlayer cohesion, as discussed earlier. In the case of PT, this influence is the largest among the evaluated parameters, as evidenced by Fig. 13. At 360 °C, a clear transition between adjacent layers is visible, which is a clear indication of the lack of interlayer cohesion. This was most likely a result of an inadequate temperature, as previously reported elsewhere [7,65]. This tendency was gradually reverted as the temperature increased, with the contrast between layers mostly disappearing in central areas of the specimen from 390 °C onwards.

Regarding defects, sections of untested samples analyzed under LOM show that higher PT values tend to result in larger voids (Fig. 14). This is most likely a consequence of coarsening effect between the voids due to the enhanced diffusion occurring at higher temperatures [71]. In this scenario, a trade-off between interlayer cohesion and defect size can be highlighted. On the one hand, colder prints provide lower interlayer cohesion, but also smaller defects; hotter prints, on the other hand, show satisfactory interlayer cohesion, at the price of having larger defects. Such a trade-off suggests that there should be a PT value where a compromise is reached and the mechanical properties are maximized, which for UTS is 386 °C (Table 6). Moreover, the trade-off can be visualized by the prediction model presented in Section 3.2, which has a statistically-significant quadratic term PT^2 (Table 5). Quadratic (or higher order) terms such as this one normally indicate the combination of two phenomena that are a function of the same factor, but influence the response in opposite directions [44]; in this case, interlayer cohesion and defect size are both a function of PT.

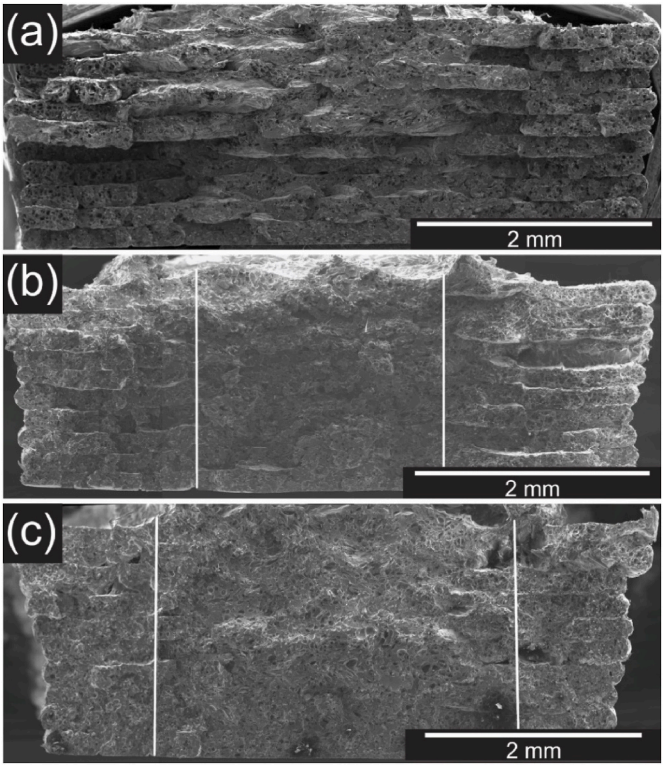

Fig. 13. Printed samples with a LH of 0.2 mm, PS of 17.5 mm/s and PT of (a) 360 °C, (b) 390 °C and (c) 420 °C.

3.5. Influence of printing speed

PS is generally considered one of the key process parameters in FFF, which can significantly influence the properties of a printed part. This has also been attested in the present study, as discussed in Section 3.2. When PS is increased, the heat input into the material decreases, since less time is spent by the extruder in a given area, resulting in a faster cooling rate. Eventually, this may cause the material to solidify more rapidly, leading to changes in the microstructure of the printed part. Microstructural differences were observed in untested samples under LOM concerning defects in the as-printed parts. The obtained results are presented in Fig. 15, with voids increasing in size at faster PS.

In terms of fracture surfaces, noticeable differences were not detected when comparing different PS conditions. Similar to observations regarding LH, specimens printed at varying PS values (Fig. 16) also exhibited a consistent pattern of having a more layered appearance towards the sides, which gradually diminished towards the center of the specimen. This effect and its magnitude did not seem to be impacted by PS itself, which suggests that this parameter did not play a strong role in

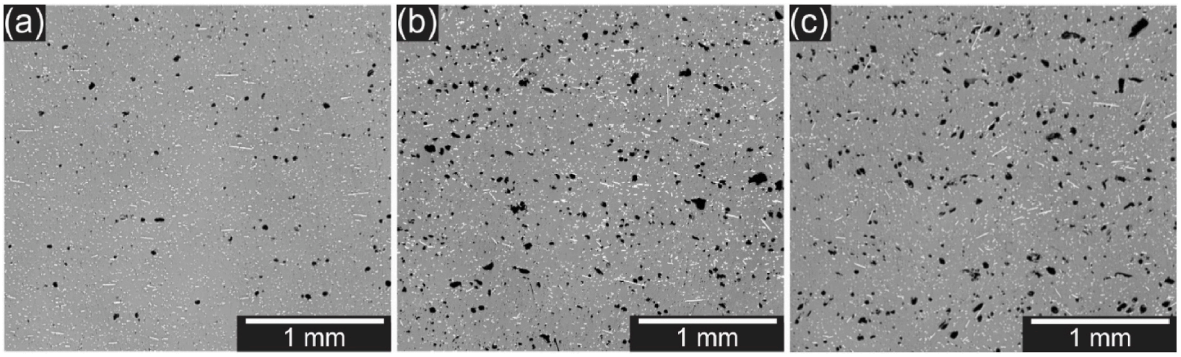

Fig. 12. Microstructure of samples printed with a PT of 390 °C, PS of 17.5 mm/s and LH of (a) 0.1 mm, (b) 0.2 mm and (c) 0.3 mm.

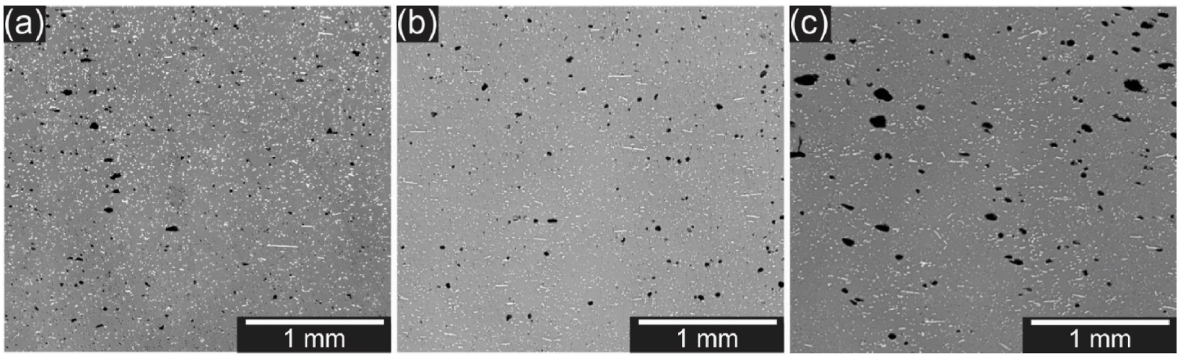

Fig. 14. Microstructure of samples printed with a LH of 0.2 mm, PS of 17.5 mm/s and PT of (a) 360 °C, (b) 390 °C and (c) 420 °C.

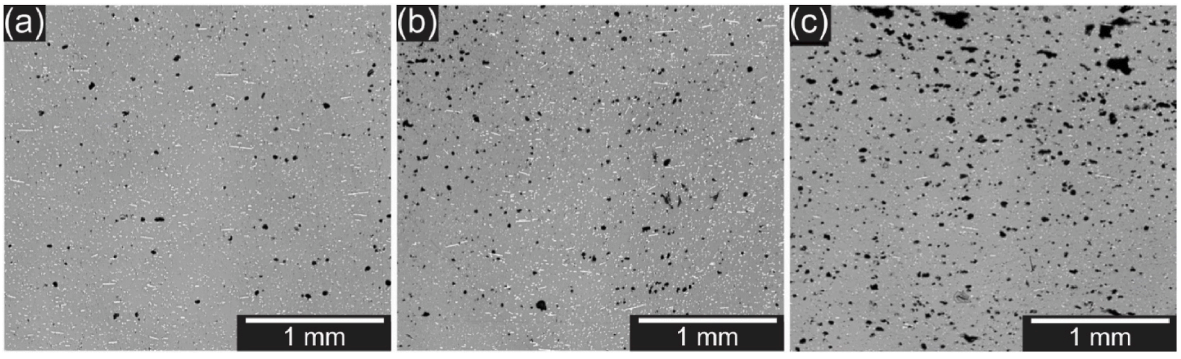

Fig. 15. Microstructure of samples printed with a LH of 0.2 mm, PT of 390 °C and PS of (a) 5 mm/s, (b) 17.5 mm/s and (c) 30 mm/s.

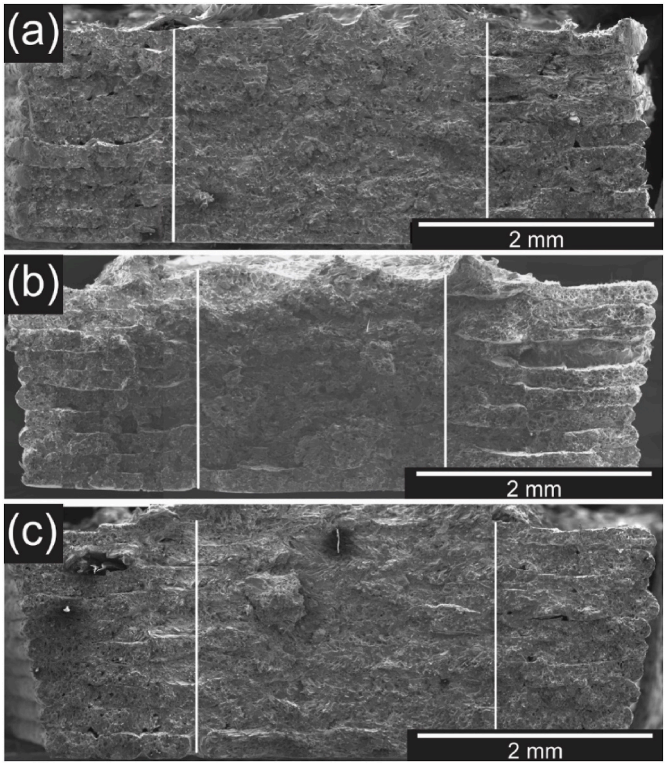

Fig. 16. Printed samples with a LH of 0.2 mm, PT of 390 °C and PS of (a) 5 mm/s, (b) 17.5 mm/s and (c) 30 mm/s.

the interlayer cohesion. Therefore, the statistical significance of this parameter on the UTS and UBS (Table 5) may have been purely a function of the size of the defects.

3.6. Fracture micromechanisms

Fracture micromechanisms themselves did not seem to be influenced by process parameters, consisting mostly of matrix failure, as well as fiber breakage and fiber pullout, with the latter being the dominant failure type. Fig. 17 presents an overview of the identified mechanisms.

As found in the literature, these fracture micromechanisms are fairly common for short fiber-reinforced thermoplastics printed by FFF, since not all the fibers are appropriately coated, resulting in poor wetting of the matrix [57,59,60]. This faulty impregnation reduces the maximum reinforcement the fibers can bear and its capability to transfer the loads adequately to the matrix, which tends to cause a predominance of fiber pullout instances (Fig. 17-(a), Fig. 17-(b) and Fig. 17-(c)) in detriment to fiber breakage ones (Fig. 17-(d)). The causes of the sub-optimal wetting have been speculated by other authors with other thermoplastic matrices and reinforcements [57,59,60], but these are beyond the scope of the present study. Moreover, while the PEEK-CF specimens experienced brittle failure macroscopically, it is possible to observe a limited degree of fibrillation around fibers, which is evidence of ductile behavior (see Fig. 14-d). Similar behavior was reported by Mbow et al. [67].

4. Conclusions

The present study investigated the fused filament fabrication (FFF) optimization and understanding for 20%-short-carbon-fiber reinforced poly-ether-ether-ketone (PEEK-20CF) taking three different loading conditions into consideration: tensile, bending and impact performance. Based on the obtained results, the following conclusions can be drawn:

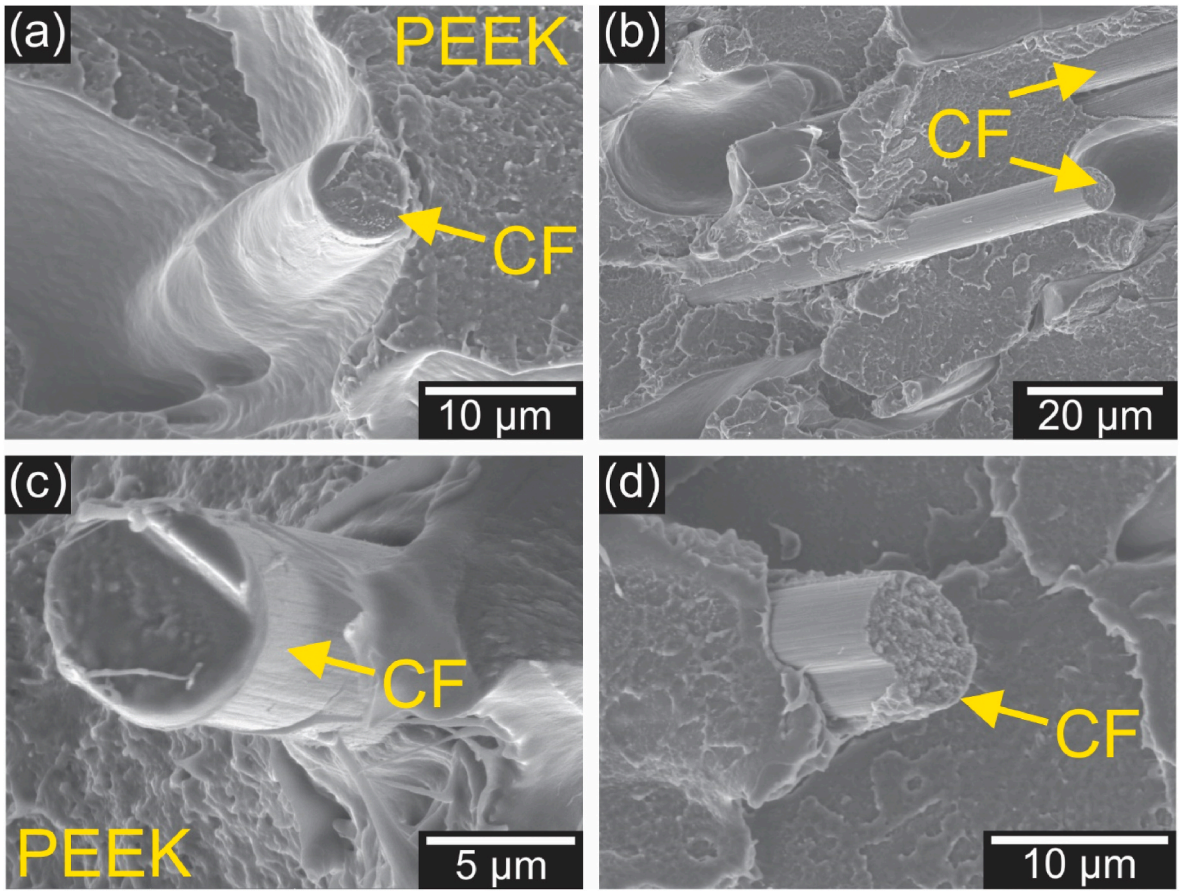

Fig. 17. Fracture micromechanisms observed in tested tensile FFF PEEK-20CF specimens printed with a LH of 0.2 mm, PT of 390 °C and PS of 17.5 mm/s: (a), (b) and (c) show fiber pullout in multiple locations and (d) fiber breakage. Matrix failure is observed in the regions around the fibers.

- The filament characterization showed a high degree of residual porosity, originating from filament production. The carbon fibers (CF) analysis showed that they presented an average diameter of 7 ± 0.5 μm, and an average fiber length of 59.7 μm, where 90% of the fibers are shorter than 100 μm. Consequently, these results indicate that although the filament used has 20 wt% CF, the full potential of this material is not explored, and the quality of filaments commercially available must be improved.
- The influence of three main FFF printing parameters – i.e., layer height (LH), printing temperature (PT) and printing speed (PS) – were evaluated for PEEK-20CF through a central composite design of experiments (CCD) for three different mechanical responses: tensile (UTS), bending (UBS), and impact (UIS) ultimate strengths. The obtained results were used to generate different regression models to predict UTS, UBS and UIS within the analyzed ranges, and analysis of variance (ANOVA) was applied to evaluate their capabilities and to determine the statistically significant factors. LH was evaluated as the most relevant parameter for UTS, followed by PS. PT showed the highest significance level for UBS and UTS, followed by PS for both cases.
- The CCD analyses combined with the obtained models were used to produce contour plots, allowing the identification of three different sets of optimized parameters for every single condition, these being: LH of 0.1 mm, PT of 385 °C and PS of 5 mm/s for UTS; LH of 0.1 mm, PT of 420 °C and PS of 5 mm/s for UBS; and LH of 0.18 mm, PT of 360 °C and PS of 30 mm/s for UIS. The optimized values reached for UTS, UBS and UIS when using these parameters were 120.1 ± 7 MPa, 179.3 ± 15 MPa and 39.2 ± 4 kJ/m^2, respectively.
- The obtained contour plots were superimposed, creating an overlaid graph that can be used to identify a feasible area in which the predicted means of all analyzed responses are within an acceptable range. Here the desired response ranges were set to be between 80 and 100% of the maximum values reached in their individual analyses. PS was fixed at the median value of 17.5 mm/s for this process, resulting in a general optimized LH and PT of 0.1 mm and 385 °C, respectively. These general optimized parameters resulted in an UTS, UBS and UIS of 116.7 ± 5 MPa, 167.2 ± 11 MPa and 28.2 ± 3 kJ/m^2.
- Finally, fractography and optical microscopy analyses were conducted to correlate the printing parameters on the material microstructure. The results showed that lower LH and PS reduce the number and size of volumetric defects observed within the printed parts, as lower values improve interlayer cohesion. Contrarily, PT showed that average values (around 385 °C) benefit the microstructure the most, as higher temperatures result in larger defects and low temperatures reduce interlayer cohesion.

Funding

The authors gratefully acknowledge financial support from the Austrian aviation program "TAKEOFF" (PILOT, grant number 852796, 2018) and the BMK – The Austrian Ministry for Climate Action, Environment, Energy, Mobility, Innovation and Technology.

Author contributions/CRediT author statement

Conceptualization, W.S.d.C. and F.M.; formal analysis, W.S.d.C., F. M. and C.B.; Funding acquisition, F.A. and S. T. A.-F.; investigation, W.S. d.C., F.M., S.P.; methodology, W.S.d.C., F.M. and S.P.; supervision, F.A. and S.T.A.-F.; writing—original draft preparation, W.S.d.C., F.M. and C. B.; writing—review and editing, W.S.d.C., F.M., C.B., S.P., F.A. and S.T.

A.-F. All authors have read and agreed to the published version of the manuscript.

Declaration of competing interest

The authors declare that they have no known competing financial interests or personal relationships that could have appeared to influence the work reported in this paper.

Data availability

Data will be made available on request.

Acknowledgments

The authors would like to acknowledge the Open Access Funding by the Graz University of Technology.

References

[1] B. Brenken, E. Barocio, A. Favaloro, V. Kunc, R.B. Pipes, Fused filament fabrication of fiber-reinforced polymers: a review, Addit. Manuf. 21 (May 2018) 1–16, https://doi.org/10.1016/J.ADDMA.2018.01.002.
[2] S. Salunkhe, S.T. Amancio Filho, J.P. Davim, Advances in Metal Additive Manufacturing, 2023, https://doi.org/10.1016/C2020-0-03745-X.
[3] P. Parandoush, D. Lin, A review on additive manufacturing of polymer-fiber composites, Compos. Struct. 182 (Dec. 2017) 36–53, https://doi.org/10.1016/J.COMPSTRUCT.2017.08.088.
[4] P. Wang, B. Zou, S. Ding, L. Li, C. Huang, Effects of FDM-3D printing parameters on mechanical properties and microstructure of CF/PEEK and GF/PEEK, Chin. J. Aeronaut. 34 (9) (Sep. 2021) 236–246, https://doi.org/10.1016/J.CJA.2020.05.040.
[5] K.R. Kumar, V. Mohanavel, K. Kiran, Mechanical properties and characterization of polylactic acid/carbon fiber composite fabricated by fused deposition modeling, J. Mater. Eng. Perform. 31 (6) (Jun. 2022) 4877–4886, https://doi.org/10.1007/S11665-021-06566-7/FIGURES/11.
[6] W. S. de Carvalho and S. T. Amancio-Filho, "Ultrasonic joining of additively manufactured metal-polymer lightweight hybrid structures," in Annual Technical Conference - ANTEC, Conference Proceedings, vol. 1, p. 526.
[7] C. Belei, J. Joeressen, S.T. Amancio-Filho, Fused-filament fabrication of short carbon fiber-reinforced polyamide: parameter optimization for improved performance under uniaxial tensile loading, Polymers 14 (7) (Mar. 2022) 1292, https://doi.org/10.3390/POLYM14071292, 2022, Vol. 14, Page 1292.
[8] A.R. Zanjanijam, I. Major, J.G. Lyons, U. Lafont, D.M. Devine, Fused filament fabrication of PEEK: a review of process-structure-property relationships, Polymers 12 (8) (Jul. 2020) 1665, https://doi.org/10.3390/POLYM12081665, 2020, Vol. 12, Page 1665.
[9] S. Salunkhe, D. Rajamani, Current trends of metal additive manufacturing in the defense, automobile, and aerospace industries, Adv. Met. Addit. Manuf. (Jan. 2023) 147–160, https://doi.org/10.1016/B978-0-323-91230-3.00004-4.
[10] G.H.M. Oliveira, C. Belei, W.S. de Carvalho, L.B. Canto, S.T. Amancio-Filho, On the fully additive manufacturing of PC/AlSi10Mg hybrid structures, Mater. Lett. 330 (Jan. 2023), 133378, https://doi.org/10.1016/J.MATLET.2022.133378.
[11] J. Kechagias, D. Chaidas, Fused Filament Fabrication Parameter Adjustments for Sustainable 3D Printing, 38, 2023, pp. 933–940, https://doi.org/10.1080/10426914.2023.2176872, 8.
[12] J.D. Kechagias, S.P. Zaoutsos, D. Chaidas, N. Vidakis, Multi-parameter optimization of PLA/coconut wood compound for fused filament fabrication using robust design, Int. J. Adv. Manuf. Technol. 119 (7–8) (Apr. 2022) 4317–4328, https://doi.org/10.1007/S00170-022-08679-2/METRICS.
[13] M. Gorelik, Additive manufacturing in the context of structural integrity, Int. J. Fatig. 94 (Jan. 2017) 168–177, https://doi.org/10.1016/J.IJFATIGUE.2016.07.005.
[14] A. Belarbi, M. Dawood, B. Acun, Sustainability of fiber-reinforced polymers (FRPs) as a construction material, Sustain. Constr. Mater. (Jan. 2016) 521–538, https://doi.org/10.1016/B978-0-08-100370-1.00020-2.
[15] A.G. Koniuszewska, J.W. Kaczmar, Application of Polymer Based Composite Materials in Transportation, 32, Feb. 2016, pp. 1–23, https://doi.org/10.1177/147776061603200101, 1.
[16] J.M. Chacón, M.A. Caminero, P.J. Núñez, E. García-Plaza, I. García-Moreno, J. M. Reverte, Additive manufacturing of continuous fibre reinforced thermoplastic composites using fused deposition modelling: effect of process parameters on mechanical properties, Compos. Sci. Technol. 181 (Sep. 2019), 107688, https://doi.org/10.1016/J.COMPSCITECH.2019.107688.
[17] W.S. De Carvalho, N.F. Colvin, A. Benatar, S.T. Amancio-Filho, Ultrasonic joining of additively manufactured metal-composite hybrid joints: a comparison between vertical and horizontal vibration modes, Met 13 (2) (Feb. 2023) 319, https://doi.org/10.3390/MET13020319, 2023, Vol. 13, Page 319.
[18] W.S. de Carvalho, S.T. Amancio-Filho, On the feasibility of joining additively-manufactured 316L stainless steel and poly-ether-ether-ketone by ultrasonic energy, Addit. Manuf. Lett. 3 (Dec. 2022), 100098, https://doi.org/10.1016/J.ADDLET.2022.100098.
[19] W.S. de Carvalho, J. Draper, T. Terrazas-Monje, A. Toumpis, A. Galloway, S. T. Amancio-Filho, Fatigue life assessment and fracture mechanisms of additively manufactured metal-fiber reinforced thermoplastic hybrid structures produced via ultrasonic joining, J. Mater. Res. Technol. (Sep. 2023), https://doi.org/10.1016/J.JMRT.2023.08.305.
[20] S.S. Yao, F.L. Jin, K.Y. Rhee, D. Hui, S.J. Park, Recent advances in carbon-fiber-reinforced thermoplastic composites: a review, Composites, Part B 142 (Jun. 2018) 241–250, https://doi.org/10.1016/J.COMPOSITESB.2017.12.007.
[21] J. Zhang, V.S. Chevali, H. Wang, C.H. Wang, Current status of carbon fibre and carbon fibre composites recycling, Composites, Part B 193 (Jul. 2020), 108053, https://doi.org/10.1016/J.COMPOSITESB.2020.108053.
[22] M.M. Mbow, P.R. Marin, F. Pourroy, Extruded diameter dependence on temperature and velocity in the fused deposition modeling process, Prog. Addit. Manuf. 5 (2) (2020) 139–152, https://doi.org/10.1007/s40964-019-00107-4.
[23] V. Pagliarulo, P. Russo, G. Leone, G.A. D'Angelo, P. Ferraro, A multimodal optical approach for investigating 3D-printed carbon PEEK composites, Opt Laser. Eng. 151 (Apr. 2022), 106888, https://doi.org/10.1016/J.OPTLASENG.2021.106888.
[24] Y. Willemin, Strong-as-steel CFRP, Reinforc Plast 65 (6) (Nov. 2021) 56–58, https://doi.org/10.1016/S0034-3617(21)00278-2.
[25] Y. Tao, et al., A review on voids of 3D printed parts by fused filament fabrication, J. Mater. Res. Technol. 15 (Nov. 2021) 4860–4879, https://doi.org/10.1016/J.JMRT.2021.10.108.
[26] M. Rinaldi, M. Ferrara, L. Pigliaru, C. Allegranza, F. Nanni, Additive manufacturing of polyether ether ketone-based composites for space application: a mini-review, CEAS Sp. J. 15 (1) (Jan. 2023) 77–87, https://doi.org/10.1007/S12567-021-00401-4/TABLES/1.
[27] T. Prater, N. Werkheiser, F. Ledbetter, D. Timucin, K. Wheeler, M. Snyder, 3D Printing in Zero G Technology Demonstration Mission: complete experimental results and summary of related material modeling efforts, Int. J. Adv. Manuf. Technol. 101 (1–4) (Mar. 2019) 391–417, https://doi.org/10.1007/S00170-018-2827-7/METRICS.
[28] D. Vaes, P. Van Puyvelde, Semi-crystalline feedstock for filament-based 3D printing of polymers, Prog. Polym. Sci. 118 (Jul. 2021), 101411, https://doi.org/10.1016/J.PROGPOLYMSCI.2021.101411.
[29] H. Wu, et al., Recent developments in polymers/polymer nanocomposites for additive manufacturing, Prog. Mater. Sci. 111 (Jun. 2020), 100638, https://doi.org/10.1016/J.PMATSCI.2020.100638.
[30] N.A. Fountas, I. Papantoniou, J.D. Kechagias, D.E. Manolakos, N.M. Vaxevanidis, Modeling and optimization of flexural properties of FDM-processed PET-G specimens using RSM and GWO algorithm, Eng. Fail. Anal. 138 (Aug. 2022), 106340, https://doi.org/10.1016/J.ENGFAILANAL.2022.106340.
[31] N.A. Fountas, J.D. Kechagias, D.E. Manolakos, N.M. Vaxevanidis, Single and multi-objective optimization of FDM-based additive manufacturing using metaheuristic algorithms, Procedia Manuf. 51 (Jan. 2020) 740–747, https://doi.org/10.1016/J.PROMFG.2020.10.104.
[32] R. Falck, S.T. Amancio-Filho, The influence of coating and adhesive layers on the mechanical performance of additively manufactured aluminum–polymer hybrid joints, Metals 13 (1) (Jan. 2023), https://doi.org/10.3390/MET13010034.
[33] M.F. Arif, H. Alhashmi, K.M. Varadarajan, J.H. Koo, A.J. Hart, S. Kumar, Multifunctional performance of carbon nanotubes and graphene nanoplatelets reinforced PEEK composites enabled via FFF additive manufacturing, Composites, Part B 184 (Mar. 2020), 107625, https://doi.org/10.1016/J.COMPOSITESB.2019.107625.
[34] J.K. Fink, High Performance Polymers, 2008, p. 609.
[35] R.I. Shekar, T.M. Kotresh, P.M.D. Rao, K. Kumar, Properties of high modulus PEEK yarns for aerospace applications, J. Appl. Polym. Sci. 112 (4) (May 2009) 2497–2510, https://doi.org/10.1002/APP.29765.
[36] D.M. Devine, J. Hahn, R.G. Richards, H. Gruner, R. Wieling, S.G. Pearce, Coating of carbon fiber-reinforced polyetheretherketone implants with titanium to improve bone apposition, J. Biomed. Mater. Res. B Appl. Biomater. 101 (4) (May 2013) 591–598, https://doi.org/10.1002/JBM.B.32861.
[37] S.M. Kurtz, J.N. Devine, PEEK biomaterials in trauma, orthopedic, and spinal implants, Biomaterials 28 (32) (Nov. 2007) 4845, https://doi.org/10.1016/J.BIOMATERIALS.2007.07.013.
[38] S. Mishra, R. Chowdhary, PEEK materials as an alternative to titanium in dental implants: a systematic review, Clin. Implant Dent. Relat. Res. 21 (1) (Feb. 2019) 208–222, https://doi.org/10.1111/CID.12706.
[39] Q. Li, W. Zhao, Y. Li, W. Yang, G. Wang, Flexural properties and fracture behavior of CF/PEEK in orthogonal building orientation by FDM: microstructure and mechanism, Polymers 11 (4) (Apr. 2019) 656, https://doi.org/10.3390/POLYM11040656, 2019, Vol. 11, Page 656.
[40] D.I. Stepashkin, F.S. Chukov, A.I. Senatov, A. M. Korsunsky Salimon, S. D. Kaloshkin, 3D-printed PEEK-carbon fiber (CF) composites: structure and thermal properties, Compos. Sci. Technol. 164 (Aug. 2018) 319–326, https://doi.org/10.1016/J.COMPSCITECH.2018.05.032.
[41] PEEK+CF20 professional carbon fiber 3D printing filament. https://www.3dxtech.com/product/carbonx-peek-cf20/. (Accessed 19 March 2023).
[42] H. Qu, et al., Influence of thermal processing conditions on mechanical and material properties of 3D printed thin-structures using PEEK material, Int. J. Precis. Eng. Manuf. 23 (6) (Jun. 2022) 689–699, https://doi.org/10.1007/S12541-022-00650-1/FIGURES/10.
[43] M. Domm, Printing of three-dimensional polymer composite structures with continuous fiber reinforcement, Struct. Prop. Addit. Manuf. Polym. Components (Jan. 2020) 333–358, https://doi.org/10.1016/B978-0-12-819535-2.00011-9.

[44] R.H. Myers, D.C. Montgomery, C.M. Anderson-Cook, Response Surface Methodology: Process and Product Optimization Using Designed Experiments, fourth ed., Wiley, 2016.
[45] W.S. de Carvalho, M.C. Vioreanu, M.R.A. Lutz, G.P. Cipriano, S.T. Amancio-Filho, The influence of tool wear on the mechanical performance of aa6061-T6 refill friction stir spot welds, Materials 14 (23) (Nov. 2021) 7252, https://doi.org/10.3390/MA14237252, 2021, Vol. 14, *Page 7252*.
[46] M. Heidari-Rarani, N. Ezati, P. Sadeghi, M.R. Badrossamay, Optimization of FDM Process Parameters for Tensile Properties of Polylactic Acid Specimens Using Taguchi Design of Experiment Method, 35, Oct. 2020, pp. 2435–2452, https://doi.org/10.1177/0892705720964560, 12.
[47] U.K. uz Zaman, E. Boesch, A. Siadat, M. Rivette, A.A. Baqai, Impact of fused deposition modeling (FDM) process parameters on strength of built parts using Taguchi's design of experiments, Int. J. Adv. Manuf. Technol. 101 (5–8) (Apr. 2019) 1215–1226, https://doi.org/10.1007/S00170-018-3014-6/METRICS.
[48] L.A. Blaga, G.P. Cipriano, A.R. Gonzalez, S.T. Amancio-Filho, Taguchi design and response surface methodology for polymer–metal joining, Join. Polym. Hybrid Struct. Princ. Appl. (Jan. 2018) 365–388, https://doi.org/10.1002/9781119429807.CH13.
[49] L.A. Blaga, G.P. Cipriano, A.R. Gonzalez, S.T. Amancio-Filho, Factorial design of experiments for polymer–metal joining, Join. Polym. Hybrid Struct. Princ. Appl. (Jan. 2018) 337–364, https://doi.org/10.1002/9781119429807.CH12.
[50] "ISO 527-2:2012(en), Plastics — Determination of tensile properties — Part 2: Test conditions for moulding and extrusion plastics." https://www.iso.org/obp/ui/#iso:std:iso:527:-2:ed-2:v1:en (accessed April. 2, 2023).
[51] "ISO 178:2019(en), Plastics — Determination of flexural properties." https://www.iso.org/obp/ui/#iso:std:iso:178:ed-6:v1:en (accessed April. 2, 2023).
[52] "ISO 179-1:2010(en), Plastics — Determination of Charpy impact properties — Part 1: Non-instrumented impact test." https://www.iso.org/obp/ui/#iso:std:iso:179:-1:ed-2:v1:en (accessed April. 2, 2023).
[53] H.R. Vanaei, S. Khelladi, A. Tcharkhtchi, Roadmap: numerical-experimental investigation and optimization of 3D-printed parts using response surface methodology, Materials 15 (20) (Oct. 2022) 7193, https://doi.org/10.3390/MA15207193, 2022, Vol. 15, *Page 7193*.
[54] A. El Magri, K. El Mabrouk, S. Vaudreuil, M. Ebn Touhami, Experimental investigation and optimization of printing parameters of 3D printed polyphenylene sulfide through response surface methodology, J. Appl. Polym. Sci. 138 (1) (Jan. 2021), 49625, https://doi.org/10.1002/APP.49625.
[55] G.P. Cipriano, L.A. Blaga, J.F. dos Santos, P. Vilaça, S.T. Amancio-Filho, Fundamentals of force-controlled friction riveting: Part II—joint global mechanical performance and energy efficiency, Materials 11 (12) (Dec. 2018) 2489, https://doi.org/10.3390/MA11122489, 2018, Vol. 11, *Page 2489*.
[56] X. Gao, N. Yu, J. Li, Influence of printing parameters and filament quality on structure and properties of polymer composite components used in the fields of automotive, Struct. Prop. Addit. Manuf. Polym. Components (Jan. 2020) 303–330, https://doi.org/10.1016/B978-0-12-819535-2.00010-7.
[57] P. Wang, et al., Preparation of short CF/GF reinforced PEEK composite filaments and their comprehensive properties evaluation for FDM-3D printing, Composites, Part B 198 (Oct. 2020), 108175, https://doi.org/10.1016/J.COMPOSITESB.2020.108175.
[58] H.L. Tekinalp, et al., Highly oriented carbon fiber–polymer composites via additive manufacturing, Compos. Sci. Technol. 105 (Dec. 2014) 144–150, https://doi.org/10.1016/J.COMPSCITECH.2014.10.009.
[59] F. Ning, W. Cong, J. Qiu, J. Wei, S. Wang, Additive manufacturing of carbon fiber reinforced thermoplastic composites using fused deposition modeling, Composites, Part B 80 (Oct. 2015) 369–378, https://doi.org/10.1016/J.COMPOSITESB.2015.06.013.
[60] E.A. Papon, A. Haque, Fracture toughness of additively manufactured carbon fiber reinforced composites, Addit. Manuf. 26 (Mar. 2019) 41–52, https://doi.org/10.1016/J.ADDMA.2018.12.010.
[61] L.H. Perng, C.J. Tsai, Y.C. Ling, Mechanism and kinetic modelling of PEEK pyrolysis by TG/MS, Polymer 40 (26) (Dec. 1999) 7321–7329, https://doi.org/10.1016/S0032-3861(99)00006-3.
[62] P. Patel, et al., Investigation of the thermal decomposition and flammability of PEEK and its carbon and glass-fibre composites, Polym. Degrad. Stabil. 96 (1) (Jan. 2011) 12–22, https://doi.org/10.1016/J.POLYMDEGRADSTAB.2010.11.009.
[63] J.N. Hay, D.J. Kemmish, Thermal decomposition of poly(aryl ether ketones), Polymer 28 (12) (Nov. 1987) 2047–2051, https://doi.org/10.1016/0032-3861(87)90039-5.
[64] C.J. Tsai, L.H. Perng, Y.C. Ling, C.J. Tsai, L.H. Perng, Y.C. Ling, A study of thermal degradation of poly(aryl-ether-ether-ketone) using stepwise pyrolysis/gas chromatography/mass spectrometry, Rapid Commun. Mass Spectrom. 11 (18) (1997) 1987–1995, https://doi.org/10.1002/(SICI)1097-0231(199712)11:18.
[65] Q. Sun, G.M. Rizvi, C.T. Bellehumeur, P. Gu, Effect of processing conditions on the bonding quality of FDM polymer filaments, Rapid Prototyp. J. 14 (2) (Mar. 2008) 72–80, https://doi.org/10.1108/13552540810862028/FULL/PDF.
[66] J. Klein, The Self-Diffusion of Polymers, 20, Nov. 2006, pp. 611–629, https://doi.org/10.1080/00107517908210929, 6.
[67] M.M. Mbow, P.R. Marin, F. Pourroy, Extruded diameter dependence on temperature and velocity in the fused deposition modeling process, Prog. Addit. Manuf. 5 (2) (Jun. 2020) 139–152, https://doi.org/10.1007/S40964-019-00107-4/.
[68] N. van de Werken, H. Tekinalp, P. Khanbolouki, S. Ozcan, A. Williams, M. Tehrani, Additively manufactured carbon fiber-reinforced composites: state of the art and perspective, Addit. Manuf. 31 (Jan. 2020), 100962, https://doi.org/10.1016/J.ADDMA.2019.100962.
[69] G.D. Goh, et al., Characterization of mechanical properties and fracture mode of additively manufactured carbon fiber and glass fiber reinforced thermoplastics, Mater. Des. 137 (Jan. 2018) 79–89, https://doi.org/10.1016/J.MATDES.2017.10.021.
[70] S. Berretta, R. Davies, Y.T. Shyng, Y. Wang, O. Ghita, Fused Deposition Modelling of high temperature polymers: exploring CNT PEEK composites, Polym. Test. 63 (Oct. 2017) 251–262, https://doi.org/10.1016/J.POLYMERTESTING.2017.08.024.
[71] X. Gao, D. Zhang, X. Wen, S. Qi, Y. Su, X. Dong, Fused deposition modeling with polyamide 1012, Rapid Prototyp. J. 25 (7) (Aug. 2019) 1145–1154, https://doi.org/10.1108/RPJ-09-2018-0258/FULL/PDF.